A search for satellite galaxies of nearby star-forming galaxies with resolved stars in LBT-SONG

Christopher T. Garling [ORCID],[1]★ Annika H. G. Peter [ORCID],[2] Christopher S. Kochanek [ORCID],[1] David J. Sand[3] and Denija Crnojević[4]

[1]*CCAPP and Department of Astronomy, The Ohio State University, 140 W. 18th Ave., Columbus, OH 43210, USA*
[2]*CCAPP, Department of Physics, and Department of Astronomy, The Ohio State University, 191 W. Woodruff Avenue, Columbus, OH 43210, USA*
[3]*Department of Astronomy and Steward Observatory, University of Arizona, 933 N. Cherry Avenue, Tucson, AZ 85719, USA*
[4]*Department of Physics, University of Tampa, 401 West Kennedy Boulevard, Tampa, FL 33606, USA*

ABSTRACT

We present results from a resolved stellar population search for dwarf satellite galaxies of six nearby ($D < 5$ Mpc), sub-Milky Way mass hosts using deep ($m \sim 27$ mag) optical imaging from the Large Binocular Telescope. We perform image simulations to quantify our detection efficiency for dwarfs over a large range in luminosity and size, and develop a fast catalogue-based emulator that includes a treatment of unresolved photometric blending. We discover no new dwarf satellites, but we recover two previously known dwarfs (DDO 113 and LV J1228+4358) with $M_V < -12$ that lie in our survey volume. We preview a new theoretical framework to predict satellite luminosity functions using analytical probability distribution functions and apply it to our sample, finding that we predict one fewer classical dwarf and one more faint dwarf ($M_V \sim -7.5$) than we find in our observational sample (i.e. the observational sample is slightly top-heavy). However, the overall number of dwarfs in the observational sample (2) is in good agreement with the theoretical expectations. Interestingly, DDO 113 shows signs of environmental quenching and LV J1228+4358 is tidally disrupting, suggesting that low-mass hosts may affect their satellites more severely than previously believed.

Key words: galaxies: dwarf – galaxies: evolution.

1 INTRODUCTION

Dwarf satellite galaxies are powerful cosmological probes on non-linear scales where there are few competing constraints, as these dwarf galaxies trace the underlying dark matter subhalo population (e.g. Zheng et al. 2005; Zheng & Weinberg 2007; Navarro 2018). In concert with galaxy evolution models for how galaxies inhabit haloes, observations of satellite luminosity functions (SLFs) can be compared to predictions from various cosmologies to place constraints on alternate dark matter models or look for deviations from the prevailing Lambda cold dark matter (ΛCDM) cosmology (e.g. Nierenberg et al. 2012, 2016; Kennedy et al. 2014; Chau, Mayer & Governato 2017; Dooley et al. 2017b; Lovell et al. 2017; Jethwa, Erkal & Belokurov 2018; Kim, Peter & Hargis 2018; Gilman et al. 2020; Lovell 2020; Nadler et al. 2020, 2021; Newton et al. 2020; Safarzadeh & Spergel 2020).

However, large uncertainties in the galaxy evolution models can make these comparisons difficult, especially as the cosmological signal (principally, the subhalo mass function, or SMF) is degenerate with the stellar mass–halo mass (SMHM) relation at fixed host mass; both can fundamentally alter the shape and normalization of the SLF. This degeneracy can be broken by sampling hosts of different masses. The SMF at infall (i.e. the unevolved SMF) in

ΛCDM scales universally with host mass, which is often described as the self-similarity of substructure in ΛCDM (e.g. Gao et al. 2004, 2012; Jiang & van den Bosch 2014, 2016). This is not true of the evolved ($z = 0$) SMF, which is affected by the tidal stripping of subhaloes and is not strictly self-similar. However, simulations show that the present-day stellar masses of dwarf satellites are closely correlated to their peak historical halo masses, which are typically their halo masses at first infall to their hosts (e.g. Reddick et al. 2013; Rodríguez-Puebla et al. 2017; Campbell et al. 2018; Behroozi et al. 2019; Buck et al. 2019; Moster et al. 2020; Wang et al. 2021). Thus, the self-similarity of substructure in ΛCDM is imprinted on the SLF. The degeneracy between the SMHM function (galaxy evolution) and the SMF (cosmology) can be broken by obtaining SLFs of hosts with a range of halo masses, as the SMHM relation will be universal across all hosts, as will the shape of the SMF, while the normalization of the SMF is dependent on the host mass (see e.g. the discussion in section 8.1 of Roberts, Nierenberg & Peter 2021). Therefore, a sample of SLFs from hosts of varied masses can be modelled simultaneously to constrain both the SMHM relation and the SMF.

Thus far, SLFs have mostly been measured for galaxies around the mass of the Milky Way (MW), as they can be easily compared to the well-studied MW satellite population, and there is a low likelihood of such galaxies hosting no detectable dwarf galaxies (e.g. Sand et al. 2014; Danieli et al. 2017; Geha et al. 2017; Müller et al. 2017, 2019; Smercina et al. 2018; Crnojević et al. 2019; Bennet et al. 2020; Carlsten et al. 2021; Mao et al. 2021). Studies at roughly

constant host mass are good for understanding halo-to-halo scatter and the environmental dependence of SLFs, but they are not optimal for understanding the SMF or the SMHM relation. Additionally, most surveys aim simply to discover new dwarfs without modelling the completeness of the search; these completeness corrections are essential to making comparisons with theoretical expectations.

An attractive approach for extending the range of host masses with measured SLFs is to go to lower host masses, as there are many nearby low-mass galaxies that can be surveyed. The dwarf galaxies associated with the Large Magellanic Cloud (LMC) found by the Dark Energy Survey (The DES Collaboration 2015a, b; Nadler et al. 2020) are a first example that low-mass galaxies host significant satellite populations, as predicted by the self-similarity of substructure in ΛCDM. Success has been found in this regime by the MADCASH project, which recently discovered new dwarf satellites of the low-mass hosts NGC 2403 (Carlin et al. 2016) and NGC 4214 (Carlin et al. 2021). The first results from the LBT-SONG survey identified two dwarf satellite candidates of NGC 628 (Davis et al. 2021). Additionally, Müller, Jerjen & Binggeli (2018) and Müller & Jerjen (2020) assembled dwarf candidate catalogues for the diffuse Leo-I and Sculptor groups, which, if confirmed, will shed light on the SLF of dwarfs in group environments, and comparison to isolated systems may reveal environmental effects on the SLF. However, larger host samples are needed to constrain the SMF and SMHM relation.

Towards this end, we present a search for dwarf satellite galaxies of six nearby (3–4.5 Mpc), sub-MW-mass hosts using imaging data from the Large Binocular Telescope (LBT; Hill et al. 2010) using the Large Binocular Camera (LBC; Ragazzoni et al. 2006; Speziali et al. 2008). These data are deep, achieving 50 per cent point-source completeness at ∼27 mag in the *B*, *V*, and *R* bands, enabling us to detect dwarf satellites as faint as $M_V \sim -7$ (or $M_* \sim 5 \times 10^4$ M$_\odot$) at roughly 50 per cent completeness by searching for dwarfs with resolved stellar populations. This sensitivity, which is better than most previous extragalactic surveys, indicates that we should be able to detect dwarfs at the transition between the classical and ultra-faint regimes. We determine our dwarf completeness function using both traditional image simulations and a novel catalogue modelling approach that explicitly includes the effects of photometric blending.

A limitation of these data relative to other SLF-focused surveys is our restricted field of view. With only a single LBC pointing per host, we generally cover only the central 400–600 kpc^2 for our hosts, while some other surveys span the entire virial volume (typically ≥1 Mpc^2 in projection). Due to our limited volume, interpretation of our results depends heavily on the assumed radial distribution of satellites. However, theoretical predictions for the radial distributions of satellites are uncertain due to tidal disruption. Resolution studies of tidal stripping have shown that satellites are artificially disrupted at resolutions typical of cosmological simulations, while analogous satellites survive much longer at higher resolution (Peñarrubia, Navarro & McConnachie 2008; Peñarrubia et al. 2010; van den Bosch & Ogiya 2018; van den Bosch et al. 2018); these objects are called orphaned subhaloes, and properly accounting for them is critical for many applications (e.g. constructing semi-analytical models of galaxy evolution and fitting the SMHM relation and the MW satellite population; Moster, Naab & White 2013; Simha & Cole 2017; Behroozi et al. 2019; Nadler et al. 2019; Drakos, Taylor & Benson 2020; Delfino et al. 2021; Jiang et al. 2021). The radial distribution is particularly susceptible to the effects of artificial disruption, as the tidal mass-loss rate is a strong function of radius. When including orphaned subhaloes, MW-scale simulations suggest that the subhalo radial distribution is even more centrally

concentrated than a cuspy dark matter host halo due to dynamical friction on the infalling satellites (e.g. Han et al. 2016). Since the strength of dynamical friction scales with the satellite halo mass (e.g. Boylan-Kolchin, Ma & Quataert 2008), the radial distribution for high-mass subhaloes is more centrally concentrated than for low-mass subhaloes (e.g. right-hand panel of fig. 3 in Han et al. 2016). Thus, the central region should have the highest surface density of satellites, and should also host many of the most massive, and easily detectable, satellites.

Most environmental quenching mechanisms are also more effective at small host-centric radii. However, the environmental processes invoked to explain the quiescent (i.e. quenched) satellite galaxies of the MW, such as accretion-shocked hot gas haloes (e.g. Birnboim & Dekel 2003; Kereš et al. 2009) and ram pressure stripping (e.g. Gunn & Gott 1972; Mayer et al. 2006; Fillingham et al. 2016; Tonnesen 2019; Stern et al. 2020), have not been explored in detail for the lower host masses we examine here. Looking for dwarf satellite galaxies at small projected radii may then shed light on the quenching mechanisms active in sub-MW-mass hosts. Using these LBT data, Garling et al. (2020) showed that the Fornax-analogue DDO 113, which ceased forming stars less than 1 Gyr ago (Weisz et al. 2011), is undisrupted and was likely quenched due to the cessation of cold gas inflows upon entering the halo of its host, the LMC-analogue NGC 4214. Similarly, Carlin et al. (2019) showed that DDO 44, a dwarf satellite of similar luminosity that also quenched about a Gyr ago (Karachentsev & Kaisin 2007; Weisz et al. 2011), was also tidally disrupted by its ∼2× LMC-mass host, NGC 2403. These results are somewhat surprising when compared to the SAGA survey, which focuses on MW-mass hosts and has found predominantly star-forming dwarf satellite galaxies (Geha et al. 2017; Mao et al. 2021). While the SAGA survey is quite different in methodology and host selection, the differences in their quenched fractions make it clear that environmental quenching mechanisms are not yet well understood.

In this work, we search for dwarf satellites of six sub-MW-mass hosts using LBT/LBC imaging, carefully derive our detection efficiency, and compare the results to theoretical expectations. We outline the acquisition and processing of our imaging data in Section 2. We present our method to search the images for dwarf satellites using resolved stars in Section 3. In Section 4, we compare two methods for deriving our observational selection function: a standard image simulation technique and a novel catalogue modelling approach that explicitly models the effects of photometric blending. In Section 5, we present the results from our search and compare them to predictions from a new theoretical framework for modelling SLFs.

2 OBSERVATIONS AND DATA REDUCTION

Our observations were originally obtained in the search for failed supernovae described in Kochanek et al. (2008), with results presented in Adams et al. (2017), Basinger et al. (2020), and Neustadt et al. (2021). This survey monitors 27 nearby, star-forming galaxies with the blue and red channels of the LBC (Ragazzoni et al. 2006; Speziali et al. 2008) on the LBT (Hill et al. 2010). The LBT has two 8.4 m primary mirrors and the LBC consists of two prime focus cameras, with one optimized for blue light and one for red. Each camera uses four 2048 × 4608 pixel CCDs with a scale of 0.225 arcsec pixel^{-1} and a field of view of 23 arcmin × 23 arcmin. The earliest data we use here were obtained in 2009 and the latest were taken in 2017. Typically two epochs of data were obtained each year. Each epoch consisted of three *R*-band exposures on LBC red paired with single *U*-, *B*-, and *V*-band exposures on LBC blue. Individual exposure times

Table 1. Summary of observations and assumed host properties.

Host	RA	Dec.	Distance (Mpc)	M_*[a] [$\log_{10}$ (M$_\odot$)]	Exposure[b] (s)	50 per cent complete[b] (mag)	Subtended area (kpc^2)	$E(B-V)$[c] (mag)
NGC 4214	12^{h}15^{m}39^s	+36°19′37″	3.04[d]	8.55 ± 0.10	1800, 1800, 5400	26.8, 26.6, 26.9	400	0.0188
IC 2574	10^{h}28^{m}23^s	+68°24′44″	3.81[d]	8.72 ± 0.14	2040, 1920, 6000	27.0, 26.6, 26.9	500	0.0311
NGC 3077	10^{h}03^{m}19^s	+68°44′02″	3.83[d]	9.17 ± 0.10	2160, 2160, 5760	27.0, 26.7, 26.9	520	0.0576
NGC 4449	12^{h}28^{m}11^s	+44°05′37″	4.02[e]	9.03 ± 0.10	3000, 3000, 8160	27.1, 26.7, 27.0	520	0.0166
NGC 4826	12^{h}56^{m}44^s	+21°40′59″	4.40[f]	10.20 ± 0.10	6480, 6480, 18 720	27.2, 26.9, 27.2	580	0.0356
NGC 4236	12^{h}16^{m}42^s	+69°27′45″	4.45[g]	9.19 ± 0.11	4080, 4320, 10 080	27.2, 26.8, 27.1	600	0.0125

[a]Leroy et al. (2019).

[b]The three values in these columns are for *B*, *V*, and *R*, respectively.

[c]Schlegel, Finkbeiner & Davis (1998) and Schlafly & Finkbeiner (2011).

[d]Dalcanton et al. (2009).

[e]Sabbi et al. (2018); see also McQuinn et al. (2010).

[f]Jacobs et al. (2009).

[g]Karachentsev et al. (2002).

were scaled to reach a fixed point-source luminosity for each galaxy (see Gerke, Kochanek & Stanek 2015) and are typically 2–4 min for the hosts studied here. Seeing varied from 0.8 to 1.5 arcsec, but we only used images with seeing better than 1.1 arcsec. We additionally exclude images with high sky brightness, which comprised roughly 5 per cent of the exposures. A summary of our observations is given in Table 1.

We reprocess the raw images for the seven closest galaxies and apply resolved star methods to search for dwarf satellite galaxies; we refer to this sample as the LBT-SONG near-sample. More distant galaxies in the sample of Kochanek et al. (2008) will be searched with integrated light methods by Davis et al. (2021, in preparation), which we will refer to as the LBT-SONG far-sample; the first results from this sample were presented in Davis et al. (2021) and revealed two dwarf satellite candidates of NGC 628. Our methods for data reduction, photometry, calibration, and artificial star tests follow closely those of Garling et al. (2020) so we abbreviate our description here, focusing mainly on changes from that analysis.

2.1 Data reduction

The IRAF MSCRED package was used to apply overscan correction, bias subtraction, and flat-fielding as described in Gerke et al. (2015). An initial astrometric calibration was made using a local installation of the astrometry.net code base (Lang et al. 2010) with custom astrometric reference files built from SDSS-DR13 (Alam et al. 2015). We then used SCAMP (Bertin 2006) to perform internal and external astrometric calibrations with focal plane distortion corrections, cross-matching the astrometry of our input images to standard deviations ∼0.1 arcsec and calibrating to *Gaia*-DR2 (Gaia Collaboration 2018) sources with similar precision.

Following this astrometric calibration, we co-added our individual exposures using SWARP (Bertin et al. 2002). Individual images were resampled using a LANCZOS3 interpolation function, and co-addition was performed with the clipped-mean algorithm from Gruen, Seitz & Bernstein (2014). Most final co-adds have seeing between 1.0 and 1.2 arcsec with a median of 1.1 arcsec.

2.2 Photometry and calibration

We performed point spread function (PSF) fitting photometry using the DAOPHOT, ALLSTAR, and ALLFRAME packages (Stetson 1987, 1994). We ran ALLSTAR in two iterations, once on the original science image and again on the science image with the sources from the

first pass subtracted to detect faint sources originally missed. We then performed forced photometry simultaneously in all bands for sources detected in at least two filters by ALLSTAR using ALLFRAME (Stetson 1994). We remove poorly measured sources by eliminating stars with photometric errors greater than 0.4 mag or χ, a measure of the goodness of fit of the model PSF, greater than 2 in the ALLFRAME catalogues. We use the DAOPHOT sharpness parameter as our statistic for separating stars and galaxies, which has been shown to work well (e.g. fig. 4 in Annunziatella et al. 2013). We classify sources with absolute values of sharpness less than 2 as stars in our final catalogue.

We calibrate our photometry by bootstrapping on to SDSS-DR13 (Alam et al. 2015) and correcting for Galactic extinction. We used relations from Jordi, Grebel & Ammon (2006) to convert SDSS magnitudes to *U*, *B*, *V*, and *R* with full error propagation. We match our photometric catalogue to the SDSS-DR13 'stars' catalogue and use the sources in common to fit zero-points and colour terms for all bands simultaneously, accounting for covariances between the zero-points and colour terms for our four bands. Mean calibration errors are 0.03−0.05 mag, determined by 10 000 iterations of bootstrap resampling. For IC 2574 and NGC 4236, we calibrated instead to PanSTARRS-DR2 (Chambers et al. 2016; Flewelling et al. 2020) due to the unavailability of SDSS-DR13 data in this regions. We use the Tonry et al. (2012) filter conversions for *B*, *V*, and *R*, and the Karaali, Bilir & Tunçel (2005) conversion for *U*, but the zero-point and colour term calibration methods remain the same.

Reported magnitudes are corrected for Galactic extinction with $E(B-V)$ values obtained by interpolating the Schlegel et al. (1998) dust maps with the updated scalings from Schlafly & Finkbeiner (2011). Hereafter, all quoted magnitudes have been corrected for Galactic extinction.

2.3 Artificial star tests

To measure our photometric errors and completeness as a function of magnitude and colour, we perform artificial star tests on our final co-adds as in Garling et al. (2020), excluding the central chips where the hosts take up a majority of the frame.

We create a mock catalogue of artificial stars on a spatial grid with a ∼15 arcsec spacing to prevent artificial crowding. We use the ADDSTAR routine from DAOPHOT (Stetson 1987, 1994) to insert the stars, which makes full use of the best-fitting analytical form of the PSF, its empirical correction table, and the spatial variation of the PSF (see Stetson 1992). We create 10 artificial images per chip per band, each with 2000 artificial stars for a total of 80 000
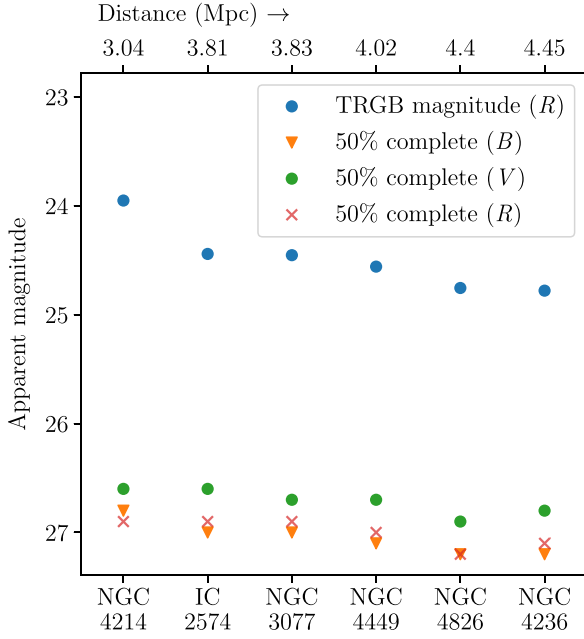
Figure 1. 50 per cent completeness values for *B*, *V*, and *R* derived from artificial star tests compared to the TRGB (absolute magnitude in *R* is -3.462) magnitude of the isochrone we use for our dwarf search. We are sensitive to $\sim$2 mag of the RGB even for the most distant hosts. Our 90 per cent completeness limits are about 1 mag brighter than our 50 per cent completeness limits.

artificial stars per host. The artificial images are processed with the same photometric pipeline as our science images and we apply the same cuts in chi, sharpness, and magnitude error to the resulting photometric catalogue. Our completeness curves for NGC 4214 are shown in fig. 1 of Garling et al. (2020), and 50 per cent completeness values for *B*, *V*, and *R* are given for each host in Table 1 and shown in Fig. 1. Our 90 per cent completeness values are generally 1 mag brighter than the 50 per cent completeness values. *U* is excluded because we do not use it for candidate detection due to its $\sim$1 mag shallower depth and the expectation that most dwarfs we are sensitive to will not have young stars that are bright in *U*.

3 DWARF SEARCH METHODS

To maximize the signal from potential dwarf galaxies and reduce contamination from foreground MW stars and background galaxies, we filter our point-source catalogues with a 10 Gyr, [Fe/H] = -2 dex isochrone from PARSEC (Aringer et al. 2009; Bressan et al. 2012; Chen et al. 2014; Marigo et al. 2017). We considered other isochrone choices, but found that using an old isochrone maximized the signal from potential candidates due to our ability to resolve the upper red giant branch (RGB). We use the filtering scheme from Garling et al. (2020), where stars are Gaussian weighted according to their proximity to the model isochrone and the photometric error from the artificial star tests. Weights range from $0 \leq w_i \leq 1$, indicating very poor and very good matches to the isochrone, respectively. We use both the $B - V$ and $V - R$ colours and we include only stars with weights greater than 0.2 to remove stars with low membership probabilities.

We then use these weights to construct a weighted kernel density estimation (KDE) using a Plummer (Plummer 1911) kernel because the Plummer model reproduces the surface brightness profiles of

MW satellites well (e.g. Muñoz et al. 2018). The value of the KDE at position $\boldsymbol{x}$ is

$$\hat{f}_{\mathrm{h}}(\boldsymbol{x}) = \sum_{i=1}^{N} w_i \, \frac{h^2}{\pi \left[h^2 + (\boldsymbol{x} - \boldsymbol{x}_i)^2 \right]^2}, \tag{1}$$

where the $\boldsymbol{x}_i$ are the positions of the stars, N is the total number of stars, h is the bandwidth of the kernel and equal to the Plummer scale radius, and the sum is over all stars $i = 1 \ldots N$ within $3h$ of $\boldsymbol{x}$.

We evaluate $\hat{f}_{\mathrm{h}}(\boldsymbol{x})$ on an 800^2 grid over the full field of view and use kernel bandwidths of 200, 300, 500, and 1000 pc at the assumed distances of our hosts to produce four maps that resemble the RGB maps common in other studies (e.g. Carlin et al. 2019). An example of a KDE map of $\hat{f}_{\mathrm{h}}(\boldsymbol{x})$ with $h = 300$ pc for NGC 4395 is shown in Fig. 2. The greatest difficulty we have to contend with is the contamination by stars from the stellar discs and haloes of the hosts, many of which are old RGB stars of the type that we hope to use to detect dwarf galaxies. Since we want to look for overdensities relative to the local background, we apply a significance mapping technique to account for this spatially varying interference.

To estimate the significance of features in our smoothed stellar density map, we apply the technique of Walsh, Willman & Jerjen (2009), which estimates the significance, *S*, of pixel *i, j* of the map *M* as the number of standard deviations above the local mean,

$$S_{i,j} = \frac{M_{i,j} - \overline{M}}{M_\sigma}, \tag{2}$$

where $\overline{M}$ and M_σ are the local mean and standard deviation of the stellar density map around pixel *i, j*, calculated using pixels within twenty times the smoothing kernel bandwidth. This is a smaller background region than many large-area surveys use, but our background varies on a sufficiently small scale that this value was found to be optimal through the image simulations discussed in Section 4.

After creating these significance maps, we create segmentation maps of contiguous regions with $S_{i,j} > 3.0$, from which we derive our candidate list. We set a minimum size for acceptance of 10 contiguous map pixels (typically $\sim$29 arcsec^2), which rejects occasional catalogue artefacts like bright stars or background galaxies shredded into multiple sources by DAOPHOT. This lower limit to detection size corresponds to a half-light radius of 55 pc or 3 arcsec at a distance of 3.8 Mpc, well below the typical size for dwarf galaxies and the size at which we expect to be able to resolve individual stars in the dwarfs. We therefore expect this limit to have a negligible effect on our ability to detect dwarfs, while allowing us to limit false detections in our candidate catalogues.

4 DWARF COMPLETENESS TESTS

For comparisons with theoretical SLFs, we need to understand our observational completeness function (or selection function) as a function of dwarf properties. In particular, the size, luminosity, star formation history (SFH), and spatial location of dwarfs are the properties that are most likely to impact our completeness. Dwarfs with half-light radii within an order of magnitude of the seeing will have most of their stars blended, making it difficult to detect individual stars, while dwarfs that are large and faint may have their signal washed out by the high density of background sources. Meanwhile, dwarfs with SFHs very different from our search isochrones may have their stars underweighted by the matched-filter algorithm, masking their signal. Finally, due to our relatively small field of view and the large angular area subtended by our hosts,
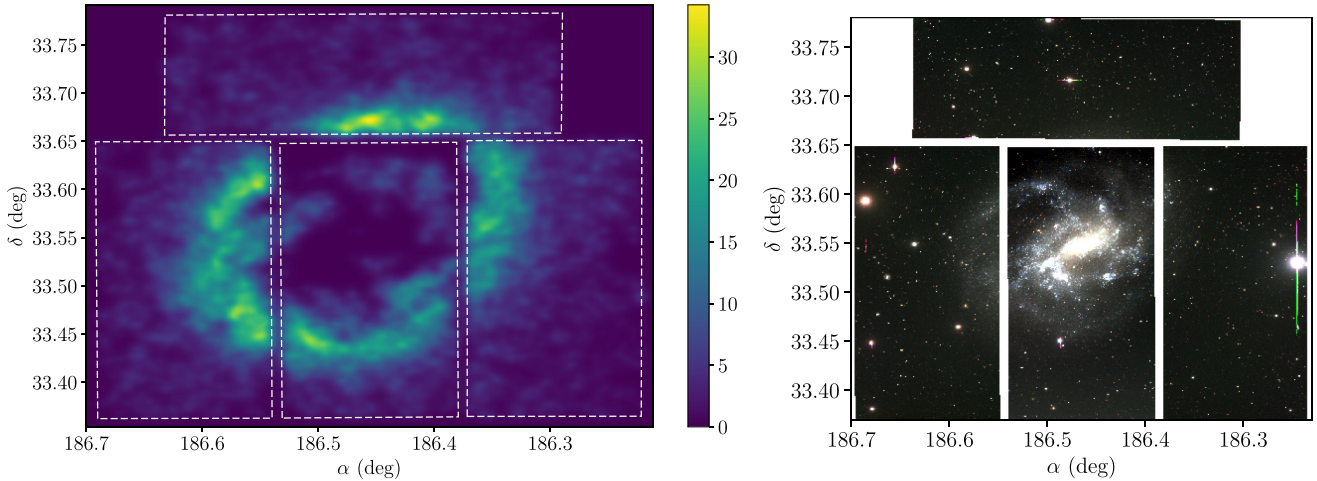
Figure 2. *Left:* KDE map for NGC 4395 with a kernel size of 300 pc. The colourbar shows raw density estimates computed from equation (1). The host lies in the central region, where our point-source photometry is poor. The bright, ring-like feature is due to stars from the host. The white, dashed boxes indicate the LBC CCD chips. *Right:* Composite colour (*R, V, B* filters mapped to RGB) of our LBT/LBC images of NGC 4395.

the background source density and its colour–magnitude diagram (CMD) vary significantly as a function of spatial position, meaning an identical dwarf will be harder to detect if it is located near the host disc than if it is near the edge of our field of view.

We use two methods to estimate our completeness – image simulations and catalogue simulations. Image simulations are the traditional approach, and they allow the most accurate measurement of detection efficiency since dwarf models are recovered from the image simulations in an identical fashion to how real candidates would be detected. However, they are computationally expensive and a full exploration of the parameter space for dwarf recovery may be prohibitive for deep, wide surveys. Catalogue simulations offer an alternative, in which all analysis is performed on the catalogue level and observational effects like photometric completeness, error, and blending must be modelled explicitly. In return for their modelling complexity, catalogue simulations are much faster, allowing a more complete sampling of the parameter space of dwarf properties. Models of the observational errors, completeness functions, and blending effects are used to generate a catalogue that approximates what would be recovered by the photometric pipeline. The dwarf detection algorithm is then applied to this processed catalogue to determine whether the simulated galaxy is recovered or not. We discuss the methods for our image simulations and the catalogue simulations separately, then compare their performance and results.

4.1 Image simulations

The image simulations are built on the same principles as those presented in section 3.1 of Garling et al. (2020) – mock galaxies are generated star by star, with positions sampled from Plummer profiles (Plummer 1911; Dejonghe 1987) and magnitudes sampled from the Chabrier (2001) lognormal initial mass function with PARSEC 1.2S isochrones (Aringer et al. 2009; Bressan et al. 2012; Chen et al. 2014), including the thermally pulsating asymptotic giant branch and other improvements from Marigo et al. (2017). We adopt the same fiducial 10 Gyr, [Fe/H] $= -2$ isochrone as used in our dwarf search for the bulk of the image simulations. Stars are sampled from the isochrone iteratively until a predetermined M_V is reached. The

full range of parameter space we explore is given in Section 4.3. We refer to this initial stellar catalogue, before any manipulation, as the 'pure' catalogue. Galactic reddening is applied and these mock galaxies are then injected into the science frames using ADDSTAR, as in the artificial star tests described in Section 2.3. We choose random positions for the dwarf galaxies to sample our spatial completeness. Stellar magnitudes and positions are shifted to the adopted distances of the hosts.

4.2 Catalogue simulations

For the catalogue simulations, we build pure dwarf star catalogues as described above. We then use probabilistic models to simulate the effects of blending, point-source completeness, and photometric error. We first simulate the effect of unresolved blending on the full, pure catalogue. Then we sample the blended catalogue randomly using the completeness functions from the artificial star tests modulated by an adjustment based on the local surface brightness. When the local surface brightness is high (as it is for compact dwarf galaxies), the completeness is reduced, accounting for the dependence of DAOPHOT's detection algorithm on the local surface brightness. We add photometric errors to the blended, completeness-sampled catalogue by sampling from the artificial star tests at the magnitudes of the catalogue stars to get the final stellar catalogue. This is embedded in a background sampled from the science images, and our full detection pipeline is run on this simulated catalogue to determine if the dwarf is detected or not.

Our catalogue simulation is similar in spirit to that of Drlica-Wagner et al. (2020), although we developed our method independently. The most important aspect where our approaches differ is in the treatment of blending. Drlica-Wagner et al. (2020) searched for satellite galaxies of the MW, and so could safely neglect blending for typical dwarf sizes. As we are searching for dwarf satellites of hosts at distances of 3–4.4 Mpc, a classical dwarf galaxy with a half-light radius of 400 pc spans only ~20 arcsec. In our ground-based imaging classical dwarfs will not be fully resolved, and anything more compact will be heavily blended. This can affect the colour, tip of the red giant branch (TRGB) magnitude, and stellar luminosity

function of the RGB. Thus, we must consider the effects of blending in order for the catalogue modelling approach to be robust.

The advantage of this technique is speed; image simulations are slow mainly because they require running photometry on each simulated image, and photometry is one of the slowest steps in our image processing pipeline. Additionally, very few stars in the image will actually be stars from the injected dwarf – thus much time is spent inefficiently re-measuring field sources. An unoptimized implementation of our algorithm in the PYTHON language shows a $100\times$ speed-up for faint dwarfs ($M_V \approx -6$), and a more moderate speedup of about $20\times$ for brighter dwarfs ($M_V \approx -10$). It is worth noting that the runtime of image simulations scales weakly with dwarf luminosity as it is nearly always the case that field sources dominate the runtime. However, as our catalogue method includes blending, it exhibits fairly strong scaling with dwarf luminosity due to the necessity of computing the projected separations of stars. A detailed efficiency analysis is beyond the scope of this work, but may be explored in future work.

4.2.1 Blending

For our purposes, we consider two types of blending: resolved blending and unresolved blending. We consider resolved blending to occur when two stars are detected and measured by the photometric pipeline, but where their PSFs overlap and light from the stars can be confused. DAOPHOT has excellent crowded-field performance, at least in part due to the fact that it measures stars simultaneously in Local Groups to account for sources with overlapping PSFs. We will assume DAOPHOT treats these situations properly and do not explicitly model this contribution – this is motivated by the fact that unresolved blending presents a much bigger problem.

We consider unresolved blending to arise when a source is detected and measured by the photometric pipeline while there is another, undetected, source contributing flux to pixels within that star's PSF. This will erroneously make the detected source brighter in each band, but if the colours of the two stars are sufficiently different it can also change the apparent colour of the detected source. If we again consider our $r_h = 400$ pc $= 20$ arcsec classical dwarf, we could only fit ~330 stars into that angular area if they are separated by one full width at half-maximum (FWHM). However, assuming a stellar mass of 10^6 M$_\odot$, comparable to Leo II or Draco (Woo, Courteau & Dekel 2008), there should be more than 10^3 stars brighter than an apparent magnitude of 27 (about our 50 per cent completeness limit) at 3.5 Mpc and more than 10^6 stars all the way down the main sequence for an old stellar population (for an observational comparison, see fig. 8 in Dolphin 2002; they have more than 5000 stars above the main-sequence turn-off for Leo II). Thus, we expect the bright RGB stars we seek to detect to have their measured magnitudes affected by many unresolved sources. We seek to understand how this affects our detection efficiency.

The likelihood of unresolved blending should depend, at minimum, on the angular distance between two sources and the seeing of the image. We also include a dependence on the magnitude difference between the stars, as it is more difficult to detect a faint star next to a bright one at fixed angular separation compared to two stars of comparable brightness. Generally there should also be a dependence on the pixel scale – at a fixed angular FWHM, a smaller pixel scale may allow the detection algorithm to separate an unresolved blend into a resolved blend. Our prescription for the likelihood of blending two stars is calibrated roughly on idealized LBT/LBC image simulations that we analysed with DAOPHOT. We
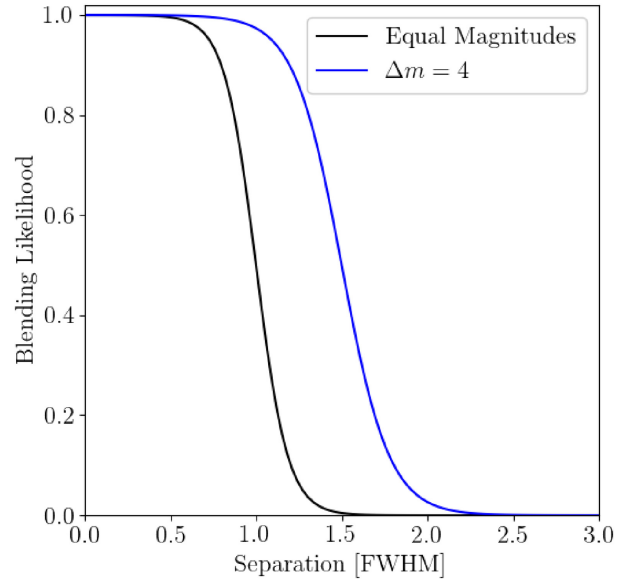

Figure 3. Estimates of the likelihood for two stars to exhibit an unresolved blend ($\mathcal{L}$ in equation 3) in our data, at two extremes: when the two stars being considered are the same magnitude (black) and when they have a difference of 4 mag.

define the probability that two stars of magnitudes m_1 and m_2 with magnitude difference $\Delta m = |m_1 - m_2|$ and an angular separation of θ will be blended as

$$\mathcal{L}(\theta) = \frac{1 + \dfrac{\exp(-m_{50})}{\rho}}{1 + \dfrac{\exp(\theta - m_{50})}{\rho}}$$

$$a(\Delta m) = \begin{cases} 1, & \text{if } \Delta m \leq 0.5 \\ 0.5\,\Delta m + 0.75, & \text{if } 0.5 < \Delta m \leq 1.5 \\ 1.5, & \text{if } 1.5 < \Delta m \end{cases}$$

$$m_{50} = a \times \text{FWHM},$$

$$\rho = a \times P/\text{FWHM}, \tag{3}$$

where FWHM is the angular FWHM of the image PSF and P is the pixel scale of the image. The factor a controls the separation at which there is a 50 per cent probability for two sources to be blended and modifies the steepness of the likelihood function. $\mathcal{L}$ becomes a step function for small values of FWHM, P, and θ, so we scale these variables together until FWHM ≥ 2 to produce a smooth curve. An estimate of $\mathcal{L}$ for our data is shown in Fig. 3.

We now describe our algorithm for blending the pure stellar catalogues. The only inputs not present in the pure catalogues are the pointwise separations θ between stars required for equation (3). For computational efficiency, the simulated CCD chips are gridded into segments of height and width equal to six times the imaging FWHM (6.6 arcsec). Blending is computed independently for each segment in the fixed grid, reducing the number of pointwise distance calculations needed for the evaluation of the blending likelihoods. In each grid segment, pointwise distances between all catalogue sources are calculated and blending is evaluated in order of ascending brightness (or, descending magnitude). The blending is assigned probabilistically according to the blending likelihood function. The new, blended source is placed at the same location as the brightest star involved in the blend (the primary source), and so supersedes this source, while the fainter star is removed from the catalogue.
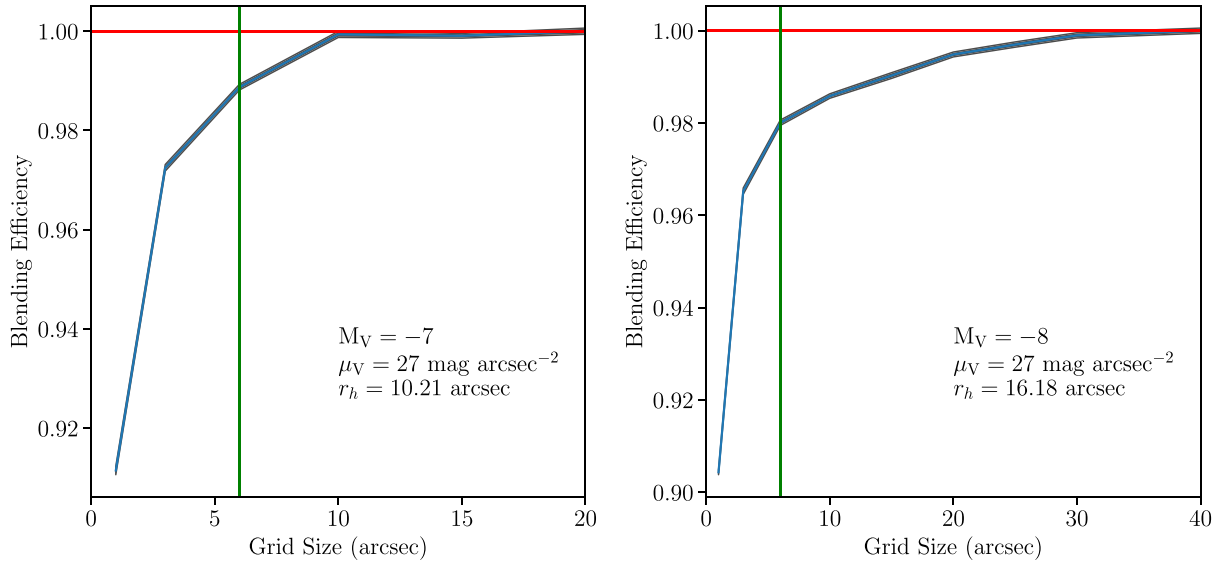
Figure 4. The efficiency of our blending algorithm as a function of the fixed grid size for two dwarf models at 3.04 Mpc. The left model has $M_V = -7$ while the right model has $M_V = -8$, and both models have $\mu_V = 27$ mag arcsec^{-2}. We define the blending efficiency to be the ratio between the number of blended stars at a particular grid size to the number of blended stars for an ungridded calculation (i.e. grid size $\geq$ galaxy size). We capture 98–99 per cent of all blends at our fiducial grid size of 6.6 arcsec. The black shaded region shows the 1σ uncertainties derived from 100 iterations performed at each grid size; run-to-run variations in blending efficiency at fixed grid size are extremely small.

This blended source may then be blended with other sources. This procedure is repeated for each grid segment until the final, blended catalogue has been produced.

Use of a fixed grid can give rise to resolution effects; in this case, stars that have small separations but lie on opposite sides of a grid line cannot be blended. Thus, use of a grid will mean stars along the grid lines may be underblended, leading to a final blending catalogue in which the number of blended stars depends on the grid size chosen. However, as the grid size decreases, fewer pointwise distances need to be computed for each grid segment, lowering per-process memory usage, and fewer pointwise distances need to be computed overall, decreasing runtime. We therefore need to strike a balance between accuracy and computational efficiency.

In Fig. 4, we show the dependence of the blending efficiency on the size of the blending grid segments, where the blending efficiency is the ratio of the number of blended stars at a particular grid size to the number of blended stars for a fully ungridded (i.e. grid size $\geq$ galaxy size) calculation. We show two model galaxies, with $M_V = -7, -8$ where both have $\mu_V = 27$ mag arcsec^{-2}. For these models, we are capturing 98–99 per cent of the blends at our fiducial grid size of 6.6 arcsec. Calculations for other models show that the higher the average stellar density within the dwarf (i.e. lower M_V or μ_V), the more deficient the blending at fixed grid size.

We show realizations of our catalogue simulation process with the fiducial grid size in Fig. 5 for dwarfs with identical absolute magnitudes but different sizes, illustrating how the surface brightness of the dwarf affects the blending calculation. As expected, we see that the more compact dwarf exhibits more unresolved photometric blending. Interestingly, the additional flux added to faint stars by unresolved blending in the compact model causes there to be more bright sources overall in the part of the CMD that we are sensitive to. However, this is mitigated by the surface-brightness-dependent completeness correction we develop in the next section, such that

similar numbers of sources are detected in both models. Thus, the most significant difference between these models is the shift of the RGB in the blended catalogue to bluer colours for the compact dwarf model due to the flux contributed from stars around the main-sequence turn-off. Reanalysing the same dwarf models used to create Fig. 5 with a larger grid size of 40 arcsec showed no noticeable changes in the blended CMD or the detection statistics, indicating that our fiducial grid size of 6.6 arcsec is sufficient to resolve the blending behaviour.

The problem of crowding has been studied statistically by Olsen, Blum & Rigaut (2003) and references therein, which give analytical formulas for the photometric errors due to blending. Given how faint our target stars are ($24 < m < 27$ mag), our measurement errors are comparable to the expected errors due to crowding for typical dwarf surface brightnesses. For example, at one magnitude below the TRGB ($m_V = 25.7$ mag), our typical photometric errors from the uncrowded artificial star tests are $\sigma_V = 0.2$ mag. For a star of the same magnitude, an equivalent error due to blending (equation 8 in Olsen et al. 2003, evaluated with the luminosity function from our model isochrone) is found at a surface brightness of 27.5 mag arcsec^{-2}, typical of the dwarfs we hope to detect. Due to the width of the matched filter used in our detection algorithm scaling with the errors in the artificial star tests, it is possible that blended stars may be scattered away from the filter by this additional source of error. However, as shown in Fig. 5, many of these blended sources still yield measurements near the model isochrone, and can therefore contribute signal to the detection algorithm.

Many other features of the blended CMDs in Fig. 5 resemble those found in earlier works (e.g. Gallart, Aparicio & Vilchez 1996; Olsen et al. 2003). Inherently blue stars (i.e. stars on the blue horizontal branch) are scattered redward while redder stars (i.e. stars on the RGB) are scattered to bluer colours due to flux contribution from stars on the upper main sequence. Intrinsically bright stars are affected less
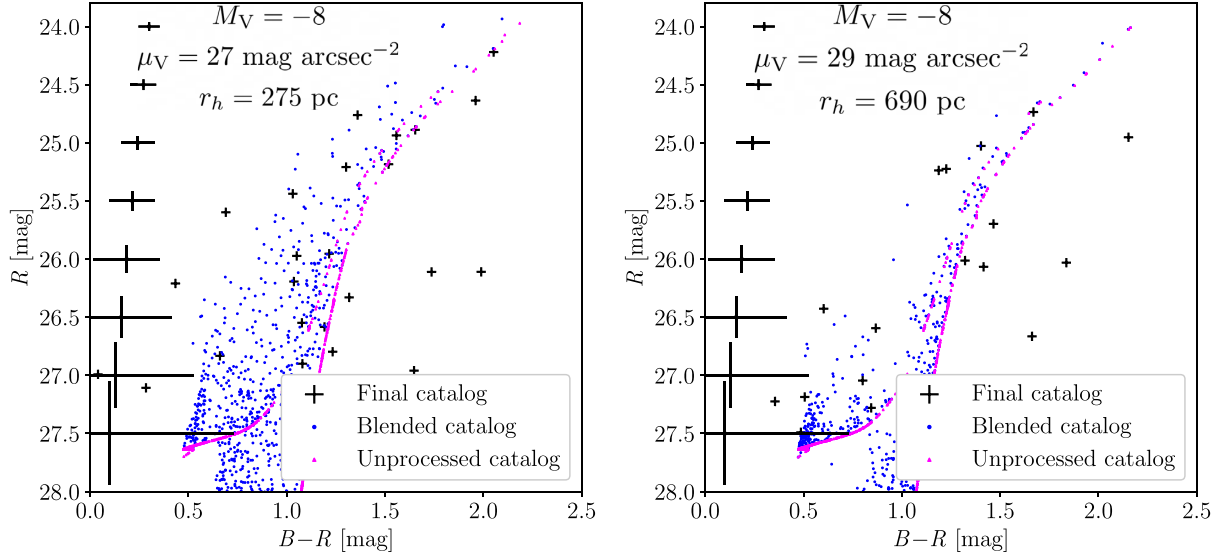
Figure 5. Comparison of different stages of the catalogue simulation process for $M_V = -8$ dwarfs of two different sizes at the distance of NGC 4214 (3.04 Mpc; our closest host). Magenta points show the pure dwarf stellar catalogue before any processing. Blue points show the stellar catalogue after blending but before application of the completeness and photometric error models. Small black crosses show the final photometric catalogue after all these steps. Median photometric errors are shown along the left-hand side of each plot. *Left:* $r_h = 275$ pc ($\mu_V = 27$ mag arcsec^{-2}; a fairly typical size for dSphs of this luminosity). Stars around the MSTO contribute most to blending, as they are numerous and bright enough to affect the magnitudes of RGB stars. The colour of the MSTO lies between $0.6 \leq B - R \leq 1$ for this model stellar population, so RGB stars are shifted to bluer colours while the blue horizontal branch shows a slight redward shift. *Right:* $r_h = 690$ pc ($\mu_V = 29$ mag arcsec^{-2}; a bit large for this luminosity). With a larger r_h, we see much less blending; as a result, there are fewer stars in our observable magnitude range because fewer stars are blended up to brighter magnitudes, but the detected stars are generally closer to the actual RGB. Some stars are scattered redward in the final catalogue due to the addition of photometric errors.

by blending than faint stars, shown by the similar TRGB magnitudes in the initial and blended catalogues and the smaller colour dispersion at the bright end of the blended RGB. Overall, our blending method captures all the main effects in the CMD noted by previous works, but further examination of the method with respect to photometric blending errors (including individual filters and colours) may be necessary in the regime where the blending errors are expected to be much greater than the basic measurement errors, such as in the study of MW globular clusters with ground-based imaging.

4.2.2 Photometric completeness effects

We now sample the blended catalogue according to the completeness functions derived from the artificial star tests. However, we cannot adopt these directly – the local surface brightness around detectable stars in our simulated dwarf galaxies will be elevated by light from unresolved stars. We refer to galaxies in this regime as being semiresolved. Generally, dwarfs with half-light radii less than 1 kpc will be semiresolved in our imaging. However, the artificial star tests presented in Section 2.3 are designed to measure photometric performance for stars in non-crowded regions, as the artificial stars are placed far apart on a regular grid. Therefore, they do not take into account local surface brightness effects and instead give results that are representative for the average surface brightness of the image (typically, the sky brightness).

To account for this shortcoming, we implement a model that decreases the photometric completeness as a function of local surface brightness in the catalogue. This model is tuned for our LBC data and calibrated from the image simulations in Section 4.1. We reduce the completeness from the artificial star tests by the multiplicative

constant

$$
C(\mu_l, \mu_s) =
\begin{cases}
\dfrac{1 + \exp(-3.5)}{1 + \exp(\mu_s - 0.8 - \mu_l)}, & \text{if } \mu_l - \mu_s \leq 2.7 \text{ mag arcsec}^{-2} \\
1, & \text{if } \mu_l - \mu_s > 2.7 \text{ mag arcsec}^{-2}
\end{cases}
\tag{4}
$$

shown in Fig. 6, where μ_l is the local surface brightness due to sources in the catalogue and μ_s is the average surface brightness of a star within its FWHM, both in mag arcsec^{-2}.

We evaluate the local surface brightness in the catalogue using the same grid as for the blending analysis to estimate the local surface brightness. Then we compute the values of our completeness functions from the artificial star tests at the magnitudes of each star in the catalogue and multiply them by the C factors for each band to find the final completeness estimates in each band. Three uniform variates are sampled for each star, and if two of them are less than the final completeness values for a star, that star is considered to be 'observed' and will be included in the final catalogue. This selection reflects the fact that we require detections in at least two bands to form our real photometric catalogues.

Finally, we add photometric errors to the stars that make it through the completeness analysis by performing a lookup against the artificial star tests. For each star, errors are sampled from artificial stars within ± 0.1 mag of the catalogue values, maintaining the full error distribution.

4.3 Completeness tests: results and comparisons

To examine our completeness as a function of the SFH, we ran a subset of image and catalogue simulations using 1 Gyr, [Fe/H] = -1; 5 Gyr, [Fe/H] = -1.5; and 10 Gyr, [Fe/H] = -2 isochrones
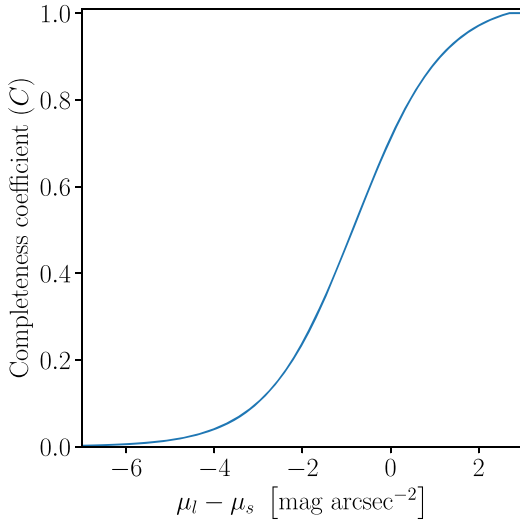
Figure 6. Value of the multiplicative constant C that modulates the completeness values from the artificial star tests as a function of the local catalogue surface brightness (μ_l) minus the average surface brightness of a star within the FWHM (μ_s). This model lessens the likelihood of observing faint stars (high μ_s) in regions of high local surface brightness (low μ_l). This constant is calibrated to the image simulations and will likely need to be recalibrated for other data sets.

to generate the mock galaxies, as these bracket the range of average dwarf SFHs. We found that the significance values from equation (2) were only affected at the ~ 10 per cent level across this range of stellar populations. Given that the FWHM of the matched filter is typically about 0.2 mag at the TRGB, we conclude that the SFHs of the dwarf galaxies have little effect on our detection efficiency. We adopt the same 10 Gyr, [Fe/H] $= -2$ isochrone from the dwarf search method for the rest of our dwarf completeness tests.

To sample our completeness in luminosity and size, we sampled galaxy luminosities uniformly from $-10 \leq M_V \leq -5$ mag and average surface brightnesses within the half-light radius log-uniformly from $25 \leq \mu_V \leq 31$ mag arcsec^{-2}. We ran 2000 image and catalogue simulations each for NGC 4214 and NGC 3077 in order to have sufficient sampling in the full two-dimensional plane of M_V and r_h to show the differences between the methods. A comparison between the image and catalogue simulations is shown in Fig. 7. The catalogue simulations show detection efficiencies that are generally smooth functions of M_V and r_h, while the image simulations show significantly more scatter. We attribute this to the image simulations being embedded in the science images, where there is a complex spatially varying background from the host. Due to this background, a galaxy that would nearly always be detected at the edge of our field may rarely be detected when it lies much closer to the host. While we sample the average background from the science images for our catalogue simulations, it is spatially uniform for each simulation and so does not capture any spatial variation of the background source density. The detection efficiencies indicate our survey should be able to find analogues of dwarf galaxies like Ursa Minor, Draco, Carina, Tucana, and Leo T.

The most interesting features to compare between the methods are the gradient with respect to the surface brightness, the surface brightness of the faintest dwarfs that can be detected with ≥ 80 per cent efficiency, and the change in the detection efficiency with respect to the half-light radius for small dwarfs. We see similar gradients with respect to the surface brightness between the catalogue and

image simulations, with both dropping fairly rapidly above 27.5 mag arcsec^{-2}. Reproducing this trend required no particular calibration of the catalogue modelling method, as the reduction in the detection efficiency is simply due to the decreasing signal to noise in the matched-filter map. The catalogue and image simulations for NGC 4214 show exactly the same combination of magnitude ($-8.5 < M_V < -8$ mag) and size ($316 < r_h < 422$ pc) for the faintest dwarfs detected with ≥ 80 per cent efficiency, while for NGC 3077 they differ by perhaps 0.5 mag and 100 pc. These matches are more difficult to reproduce, as the completeness limit depends on the density of the background and the treatment of blending. If we neglect blending entirely in the catalogue modelling, the completeness limit moves to smaller sizes and fainter magnitudes, substantially biasing our estimates in this regime. Our treatment of blending is also critical for reproducing the decrease in the detection efficiency with respect to the half-light radius as we move to small sizes; this is the most difficult feature to match. Both the catalogue-level blending and the surface-brightness-dependent completeness correction are needed to reproduce the decrease in detection efficiency measured in the image simulations, but they do surprisingly well. A particularly interesting result in the NGC 4214 simulations is that we simultaneously reproduce the steep drop in detection efficiency for dwarfs with $-8.5 < M_V < -8$ inside of 316 pc and the much shallower drop for dwarfs with $-8 < M_V < -7$, with the peak detection efficiency at fixed M_V occurring at the same radius with both methods. With good agreement between the catalogue and image simulations for all of these features, we use catalogue simulations to derive the detection efficiencies for the rest of our hosts since they are much faster to compute compared to image simulations. Improving the background modelling is one of the main areas where we hope to improve the catalogue simulations in the future.

5 RESULTS

5.1 Observational results

After candidates are identified using the procedures outlined in Section 3, we validate the detections with a combination of visual inspection and structural parameter estimation. The visual inspection checks that the candidate is not an obvious false detection, like a large background galaxy shredded into many point sources by DAOPHOT. If the detection does not appear to be due to an artefact, we attempt to measure its structure using an elliptical Plummer model with the maximum-likelihood approach presented in Martin, de Jong & Rix (2008). We detect an average of four artefacts and three candidates per host, including two previously known dwarf galaxies, DDO 113, a satellite of NGC 4214, and LV J1228+4358, a satellite of NGC 4449. Most other candidates show a relatively flat spatial profile consistent with a chance arrangement of point sources matching the filtered isochrone. There are a few candidates that show some spatial clustering of point sources that might indicate the presence of a dwarf galaxy, but comparison with dwarfs of similar size from the image simulations described in Section 4.1 reveals that we should expect detectable diffuse emission from these candidates, but we detect none. These candidates are most likely background galaxy clusters or groups of red galaxies. Analysis of the luminosity function of the point sources detected in these candidates also shows that there are more bright sources than we would expect at the distances of our hosts, further supporting this interpretation. An example of one such false detection is shown in Fig. 8.

We also performed a full visual inspection of the images, focusing especially on small candidates, as our resolved-star search method
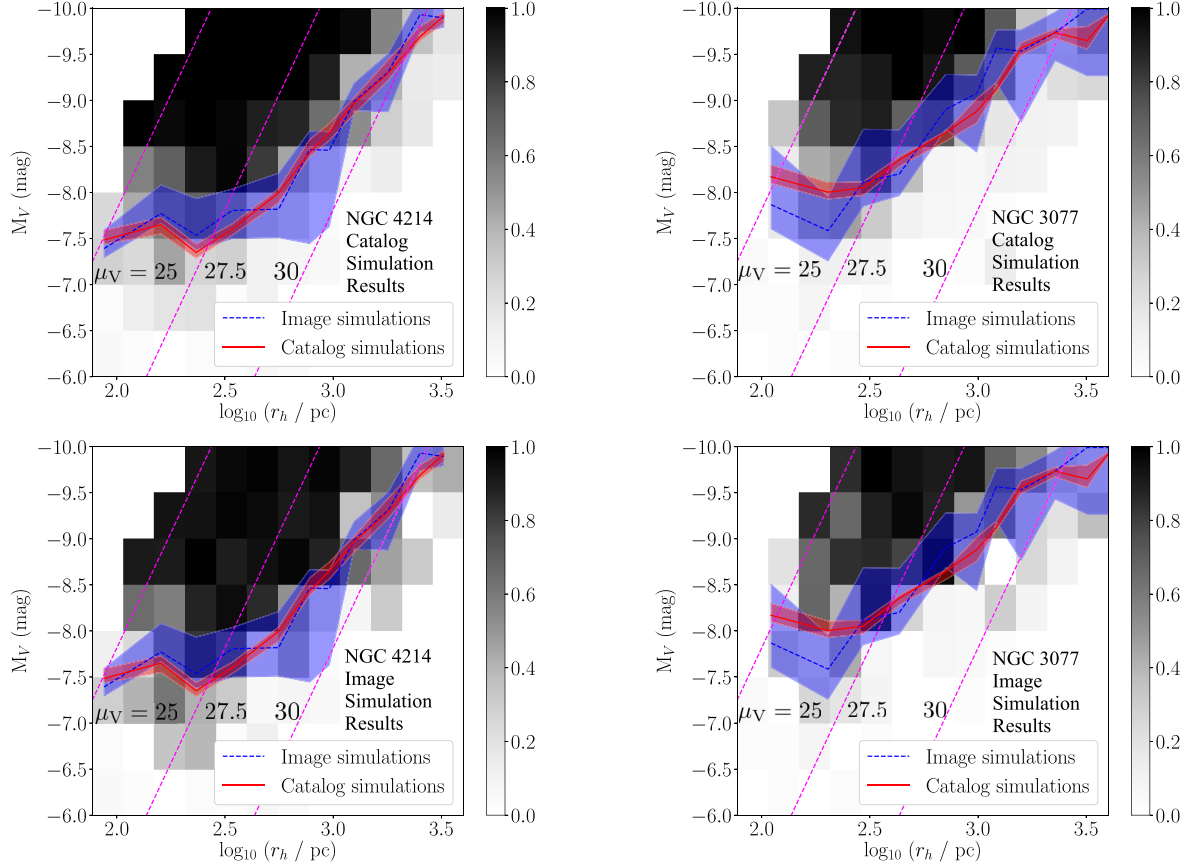
Figure 7. Results of catalogue simulations (top row) and image simulations (bottom row) for NGC 4214 (left-hand column) and NGC 3077 (right-hand column). Approximate 50 per cent completeness curves are overlaid with statistical uncertainty ranges. Lines of constant surface brightnesses of 25, 27.5, and 30 mag arcsec^{-2} inside the half-light radius are shown in pink. Bins become darker following the colourbars as the completeness increases. The catalogue simulations show more uniformity overall; they are nearly monotonically increasing to higher luminosities and smaller sizes. The image simulations show considerably more variation, which we attribute to variance in the detection efficiency with dwarf position. The catalogue simulations use spatially uniform backgrounds for each realization, while the image simulations include the large local variations in the background due to contamination from stars belonging to the host.
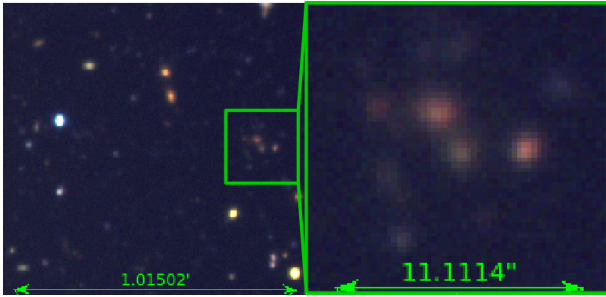

Figure 8. Example of a false positive. The left-hand panel shows a ~1 arcmin field of view to illustrate the typical point-source density in this region, and the detection is enclosed within a square. In the right-hand panel, we show a zoom-in on this detection region. The point sources here have colours close to our model isochrone, and they are close together, so our algorithm reports this as a dwarf galaxy candidate. However, we would expect to see unresolved emission for a dwarf galaxy of this size, but we detect none, and the point sources show no coherent radial density structure, leading to its rejection.

loses some detection capability for dwarfs smaller than ~200 pc (see Fig. 7) due to the strong blending in these galaxies. To guide our visual search, we generated 42 image simulations for each host as in Section 4.1 of dwarfs from $-10 \leq M_V \leq -5$ mag and $25 \leq$ $\mu_V \leq 31$ mag arcsec^{-2}. Examples of these model dwarf galaxies are shown in Fig. 9. These image simulations illustrate the expected visual appearance of any dwarfs, particularly how well resolved they are at the distance of each host. We find an abundance of low surface brightness galaxies in our imaging, but they all have light profiles far smoother than we would expect if they were at distances of 3–4.5 Mpc. We identify no significant dwarf satellite candidates from this visual search.

We therefore consider only two satellite dwarf galaxies to have been found in our imaging survey, both of which were previously known: DDO 113, which is a satellite of NGC 4214 and was examined in Garling et al. (2020), and LV J1228+4358, which is a large, disrupting (Martínez-Delgado et al. 2012; Rich et al. 2012; Toloba et al. 2016) satellite of NGC 4449. Both of these dwarfs are easily identified by our detection algorithm, with estimated detection efficiencies of 100 per cent. Since LV J1228+4358 is in the process of tidal disruption, we must consider whether it should be characterized as a galaxy or a stream for the purposes of this analysis. Given that it appears to have a centrally concentrated stellar component that may still be bound (Martínez-Delgado et al. 2012), we choose to treat it as a galaxy and include it in our theoretical analysis. It is worth noting that DDO 113 also shows evidence for interaction with its host, as its star formation was quenched about 1 Gyr ago (Weisz et al. 2011), likely because of cessation of cold gas
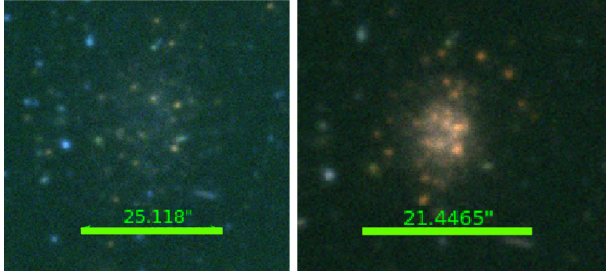
Figure 9. Examples of the simulated dwarf galaxies used to derive our detection efficiency (second row of Fig. 7) and to guide our visual inspections for NGC 4214. *Left:* A $M_V = -8$, $r_h = 280$ pc (19 arcsec) dwarf, for which we are ~ 50 per cent complete averaged over the full field. In regions of low source density (i.e. far from the host), we are significantly more complete, but such galaxies are rapidly lost near the host. There is some unresolved emission that can be visible depending on the local background level, and typically $10-20$ detectable RGB stars, although stochasticity in the IMF sampling affects our detection efficiency. *Right:* A $M_V = -8$, $r_h = 110$ pc dwarf (7.5 arcsec). Compared to the more diffuse dwarf, much more unresolved light is visible, but the centre of the galaxy is badly blended and so the detection efficiency with the point-source algorithm is worse. We expect our visual inspection to help with the identification of these kinds of galaxies.

inflows after its infall to NGC 4214 (Garling et al. 2020). Thus, we may be seeing signatures that low-mass hosts affect their satellites more strongly than previously believed.

We adopt the measurements from Garling et al. (2020) for DDO 113, namely $m_V = 15.17$ mag, so that its intrinsic luminosity is $M_V = -12.17$ at the TRGB-measured distance of 2.95 Mpc (Dalcanton et al. 2009). There is a measurement of $m_B = 14.2$ for LV J1228+4358 in Karachentsev, Makarov & Kaisina (2013), while Carlsten et al. (2019) measure $m_g = 16.50$ and $m_i = 15.95$, and Rich et al. (2012) and Martínez-Delgado et al. (2012) both find $M_r = -13.5$, $M_g = -13.05$. From our own imaging, we measure $m_B = 15.69$ ($M_B = -12.35$) and $m_V = 14.99$ ($M_V = -13.03$) by fitting Sérsic profiles using GALFITM (Häußler et al. 2013), which is a multiband extension of GALFIT (Peng et al. 2010); we perform this fitting analogously to the procedure described in section 3.1 of Garling et al. (2020). While the Karachentsev et al. (2013) apparent magnitude is discrepant from our own, our photometry is consistent with the photometry of Rich et al. (2012), Martínez-Delgado et al. (2012), and Carlsten et al. (2019) given the Jordi et al. (2006) filter conversions. We adopt our measured quantities for LV J1228+4358 for the theoretical work in Section 5.2 Additional photometry and structural parameters are given in Table 2. The structural parameters for LV J1228+4358 have large uncertainties due its irregular morphology.

5.2 Theoretical results

Here, we present theoretical expectations for the cumulative SLF, both intrinsic and observed, of the LBT-SONG near-sample. We derive these expectations based on an expanded version of the Bayesian method presented in Dooley et al. (2017a); this expanded formalism will be presented in an upcoming paper along with a theoretical interpretation of the full LBT-SONG sample. In brief, the method formulates a distribution function $dN/dM_V(M_V|\Theta)$ that can be integrated to yield the cumulative SLF, $N < M_V(M_V|\Theta)$, where Θ are model parameters. For this first analysis, we adopt a single set of model parameters, but we will explore other models in future work.

Table 2. Summary of GALFITM photometry and Sèrsic structural parameters for detected dwarf satellites.

Parameter	Value	Uncertainty	Reference
		DDO 113	
Host	NGC 4214		
RA	$12^h14^m58.3^s$	$0.^s1$	Garling et al. (2020)
Dec.	$+36°13'07''$	$2''$	Garling et al. (2020)
$m_{U,0}$	15.62	0.10	Garling et al. (2020)
$m_{B,0}$	15.66	0.10	Garling et al. (2020)
$m_{V,0}$	15.16	0.10	Garling et al. (2020)
$m_{R,0}$	15.09	0.10	Garling et al. (2020)
D	2.95 Mpc	0.083 Mpc	Dalcanton et al. (2009)
M_V	-12.19	0.18	
R_e	43.6 arcsec	1.5 arcsec	Garling et al. (2020)
	624 pc	21 pc	Garling et al. (2020)
n	0.64	0.02	Garling et al. (2020)
q	0.63	0.05	Garling et al. (2020)
		LV J1228+4358	
Host	NGC 4449		
RA	$12^h28^m44.^s8$	$0.^s1$	This work
Dec.	$+43°58'06''$	$4''$	This work
$m_{B,0}$	15.69	0.20	This work
$m_{V,0}$	14.99	0.20	This work
$m_{R,0}$	15.11	0.20	This work
D	4.07 Mpc		Karachentsev et al. (2013)
M_V	-13.03	0.20	
R_e	67 arcsec	10 arcsec	This work
	1300 pc	200 pc	This work
n	0.62	0.10	This work
q	0.28	0.06	This work

(i) We start with the Moster et al. (2013) SMHM relation and assume a constant scatter in the relation of 0.2 dex (Behroozi, Wechsler & Conroy 2013; Garrison-Kimmel et al. 2017), from which we form the probability distribution function (PDF) for the host halo mass given its observed stellar mass and uncertainty (see Table 1).

(ii) We adopt the Dooley et al. (2017a) SMF, which gives the distribution $dN/dM_{sub}(M_{sub}|M_{host})$ that describes the subhalo number distribution as a function of the host's halo mass. Marginalizing the product of the host halo mass PDF and the SMF over the host halo mass gives the mean SMF predicted for the host. We can transform this into observational units given the PDF for a subhalo of mass M_{sub} to host a galaxy of luminosity M_V.

(iii) We adopt the reionization quenching model of Dooley et al. (2017a) to describe the likelihood that a subhalo of a given halo mass hosts a luminous stellar component.

(iv) We then use the same SMHM relation and scatter described above to form subhalo stellar mass distributions given the halo masses.

(v) We next adopt the colour–stellar mass-to-light ratio relation with scatter from García-Benito et al. (2019) to model the PDF of the stellar mass-to-light ratio as a function of colour, and the empirical satellite colour distribution from SAGA (Mao et al. 2021). Combining these allows us to construct a model PDF for the luminosity (M_V) of a satellite given its colour and stellar mass.

Marginalization over the host halo and stellar masses, and the satellite halo masses, stellar masses, and colours yields $dN/dM_V(M_V|\Theta)$, which is then integrated to give the expected mean, intrinsic, cumulative SLF for each individual host.

We account for observational incompleteness in two steps: first accounting for photometric incompleteness within the field of view,

then for the restricted field of view of our imaging. We can account for photometric incompleteness by using the fake galaxy tests conducted in Section 4, but we must include a treatment of dwarf galaxy size in the theoretical calculation to match the r_h axis of our completeness tests. We estimate satellite galaxy sizes by adopting the simple model relating galaxy size to halo virial radius given by equation (6) in Jiang et al. (2019), $R_{e,3D} = 0.02(c/10)^{-0.7} R_{vir}$, where c is the halo concentration. However, converting $R_{e,3D}$ to 2D requires additional prefactors to account for projection effects (f_p) and a conversion from mass weighting, which is used to derive $R_{e,3D}$ in simulations, to light weighting, which is used observationally (f_k), such that $R_{e,2D} = f_k f_p R_{e,3D}$. We adopt $f_k f_p = 0.78$ as in Somerville et al. (2018), which is derived for predominantly spherical systems. Jiang et al. (2019) estimates a scatter in the galaxy size–virial radius relation of 0.18 dex, but we adopt 0.3 dex to account for random viewing angles and a range of possible galaxy shapes (e.g. additional spread in the $f_k f_p$ prefactor). We use the Child et al. (2018) concentration–mass relations, which are derived from dark-matter-only simulations assuming the WMAP-7 (Komatsu et al. 2011) cosmology. During the integration, we parse the completeness tables and multiply our detection probability as a function of M_V and r_h into the joint PDF.

To account for our restricted field of view, we assume the radial distribution of satellites follows the mass distribution of the host halo. Han et al. (2016) showed that, when tracking all orphaned subhaloes, the final radial distribution is more concentrated than the host halo. We assume some fraction of the orphaned satellites tracked into the inner halo in Han et al. (2016) and used to assemble their radial distribution will be disrupted and hence undetectable in real data. Additionally, our model is fairly similar to the observed radial distribution of satellites of the MW (e.g. fig. 1 in Kim et al. 2018; see also Carlsten et al. 2020). Correcting our distributions then amounts to calculating the fractions of the total host virial masses enclosed within our projected fields of view, and multiplying our distributions by these fractions. This treatment neglects possible splashback scenarios (e.g. More, Diemer & Kravtsov 2015; Diemer 2021) by implicitly assuming that the virial radius is the halo boundary, but the internal consistency of the calculation is maintained as long as the same halo boundary is used for the calculation of the radial distribution and the SMF. Moreover, these corrections are small; including subhaloes out to the splashback radius along the line of sight yields a ~ 5 per cent increase in expected satellite detections for a search over the full virial volume of the host, while the correction is negligible for our field of view (fig. 11 in Dooley et al. 2017a). With this last correction, we produce the final estimates for the mean SLFs of the hosts in the LBT-SONG near-sample; the cumulative SLF for the entire host sample is shown in Fig. 10. To estimate the intrinsic variance we should expect in our sample, we assume the SMF is negative binomial distributed as in Boylan-Kolchin et al. (2010). We sample random SLFs from each host independently and sum them to form Monte Carlo realizations of the theoretical SLFs. The 1σ range of these samples is indicated by the shaded region in Fig. 10.

The total number of dwarfs (2) is in good agreement between the data and the theoretical expectations, but the observed SLF has more classical dwarfs than expected, lying outside the 1σ range for dwarfs with $M_V < -10$. We find that only 4 per cent of our simulated samples contain two dwarfs brighter than -12 mag, as we find in our observational sample. Additionally, 55 per cent of simulated samples have at least one dwarf fainter than -10 mag, while we find none in our observations. This disagreement in the shape of the SLFs is reflected in the results of the two-sample Kolmogorov–Smirnov test, which uses normalized cumulative distributions to estimate the probability that two samples are drawn from the same distribution.
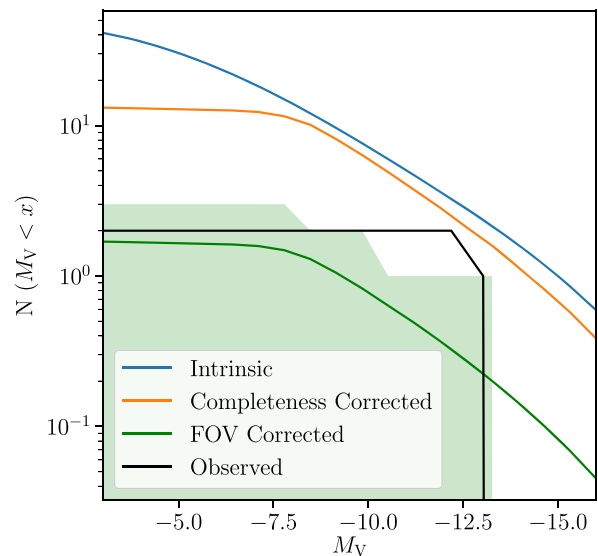

Figure 10. Theoretical expectations for the cumulative SLF of the hosts in the LBT-SONG near-sample. We show the intrinsic SLF in blue, while the orange line shows the whole-halo expectation given our photometric completeness limits, and the green line gives the final expectation after factoring in our restricted field of view. The shaded region around the final expectation shows the 1σ range of SLFs from random samples given the expectation value. Our observed dwarf satellite sample, consisting of DDO 113 and LV J1228+4358, is shown in black.

Comparing our Monte Carlo samples to our observational sample, we find a probability of 0.07 that they are drawn from the same distribution (i.e. that the observational SLF matches the theoretical SLF). An internal comparison between the Monte Carlo samples shows that only 5 per cent of the samples have probabilities equal to or less than 0.07. From these comparisons, we find that the observational SLF is top-heavy compared to the theoretical expectations with discrepancy in the shape of the SLF at the 1.5σ level. Remember, however, that we are working with a small observational sample, as we surveyed only six hosts and covered only a small fraction of their virial volumes. Considering the good agreement between the theory and observations in the total number of dwarfs, we conclude that the observations match the theoretical expectations reasonably well. Further theoretical work after adding the LBT-SONG far-sample to our data will allow us to draw stronger conclusions.

6 CONCLUSION

In this work, we presented observational results from the LBT-SONG near-sample, which utilizes deep ($m \sim 27$ mag) LBT/LBC images to search for dwarf satellites of six nearby, star-forming galaxies. We search for dwarfs as clustered point sources and characterize our detection efficiency using a combination of image simulations and a new catalogue modelling technique that explicitly models the blending of stars. We show that the catalogue modelling technique, after calibration to image simulations, serves as an excellent emulator for the detection efficiency with greatly reduced computational cost, and that treatment of unresolved blending is crucial for application of this method in the semiresolved regime. We argue that similar analyses of detection efficiency should become standard in the field of luminosity function measurements, in particular exploration of the

effects of both size and luminosity, as detection efficiency drops at fixed M_V for increasing r_h.

From our search, we find no new dwarf satellites, but we recover two previously known classical dwarf satellites. We present new photometric and morphological measurements of LV J1228+4358, an apparently disrupting dwarf of NGC 4449. Adding in DDO 113, a dwarf of NGC 4214 previously studied in Garling et al. (2020), our observational sample of dwarf satellites consists of two classical dwarfs. Interestingly, both of these dwarfs show signs of environmental interactions with their hosts. The star formation in DDO 113 was quenched about 1 Gyr ago (Weisz et al. 2011), likely by strangulation (Garling et al. 2020), the cessation of cold gas inflows following accretion of the dwarf by the host, while LV J1228+4358 shows photometric irregularities most easily explained by tidal disruption (e.g. Martínez-Delgado et al. 2012; Rich et al. 2012; Toloba et al. 2016). For both of our observed dwarfs to have such distinct signatures of host interactions indicates that sub-MW-mass hosts may affect their satellite galaxies more strongly than previously thought.

Finally, we preview a new theoretical framework for predicting SLFs from theory and compute the mean expected SLF for the LBT-SONG near-sample. This phenomenological approach combines theoretical models for halo mass functions and SMFs with empirical models for the galaxy–halo connection and secondary galaxy properties to formulate a joint PDF that can be marginalized over to produce mean expected SLFs, and sampled to produce mock systems. We further correct for our photometric incompleteness using our dwarf detection efficiency measurements and our restricted field of view, producing expectation values that properly account for our observational limitations. We find that our theoretical expectation, in comparison to the observational sample, has one fewer classical dwarf and one more faint dwarf of $M_V \sim -7.5$ (i.e. the observational sample is top-heavy). However, overall agreement between the observational and theoretical results is reasonable given the small sample size. We expect to be able to draw stronger conclusions when we add the LBT-SONG far-sample into our theoretical analysis.

Our framework is well suited to interpret observational results from current and future surveys, such as SAGA (Geha et al. 2017; Mao et al. 2021) and MADCASH (Carlin et al. 2016, 2021), which have and will continue to measure SLFs for large samples of hosts. The simulation-based work that is often done to compare the MW's dwarf satellite population to theory (e.g. Nadler et al. 2020) provides more detail than our method, but it is also much more computationally expensive and so calculating expectations for large ensembles of hosts is less viable. It is also difficult to vary the cosmology since it requires the simulation to be rerun. As our framework uses fully analytical models, it is highly extensible to alternate cosmologies and galaxy evolution models. A paper detailing this framework in full and exploring the impact of model choice is in preparation, which will follow the observational paper detailing the search for satellites in the LBT-SONG far-sample using integrated light detection methods.

DATA AVAILABILITY

The data underlying this article are proprietary but may be shared on reasonable request to the corresponding author.

REFERENCES

Adams S. M., Kochanek C. S., Gerke J. R., Stanek K. Z., 2017, MNRAS, 469, 1445

Alam S. et al., 2015, ApJS, 219, 12

Annunziatella M., Mercurio A., Brescia M., Cavuoti S., Longo G., 2013, PASP, 125, 68

Aringer B., Girardi L., Nowotny W., Marigo P., Lederer M. T., 2009, A&A, 503, 913

Basinger C. M., Kochanek C. S., Adams S. M., Dai X., Stanek K. Z., 2020, preprint (arXiv:2007.15658)

Behroozi P. S., Wechsler R. H., Conroy C., 2013, ApJ, 770, 57

Behroozi P., Wechsler R. H., Hearin A. P., Conroy C., 2019, MNRAS, 488, 3143

Bennet P., Sand D. J., Crnojević D., Spekkens K., Karunakaran A., Zaritsky D., Mutlu-Pakdil B., 2020, ApJ, 893, L9

Bertin E., 2006, in Gabriel C., Arviset C., Ponz D., Enrique S., eds, ASP Conf. Ser. Vol. 351, Astronomical Data Analysis Software and Systems XV. Astron. Soc. Pac., San Francisco, p. 112

Bertin E., Mellier Y., Radovich M., Missonnier G., Didelon P., Morin B., 2002, in Bohlender D. A., Durand D., Handley T. H., eds, ASP Conf. Ser. Vol. 281, Astronomical Data Analysis Software and Systems XI. Astron. Soc. Pac., San Francisco, p. 228

Birnboim Y., Dekel A., 2003, MNRAS, 345, 349

Boylan-Kolchin M., Ma C.-P., Quataert E., 2008, MNRAS, 383, 93

Boylan-Kolchin M., Springel V., White S. D. M., Jenkins A., 2010, MNRAS, 406, 896

Bressan A., Marigo P., Girardi L., Salasnich B., Dal Cero C., Rubele S., Nanni A., 2012, MNRAS, 427, 127

Buck T., Macciò A. V., Dutton A. A., Obreja A., Frings J., 2019, MNRAS, 483, 1314

Campbell D., van den Bosch F. C., Padmanabhan N., Mao Y.-Y., Zentner A. R., Lange J. U., Jiang F., Villarreal A., 2018, MNRAS, 477, 359

Carlin J. L. et al., 2016, ApJ, 828, L5

Carlin J. L. et al., 2019, ApJ, 886, 109

Carlin J. L. et al., 2021, ApJ, 909, 211

Carlsten S. G., Beaton R. L., Greco J. P., Greene J. E., 2019, ApJ, 879, 13

Carlsten S. G., Greene J. E., Peter A. H. G., Greco J. P., Beaton R. L., 2020, ApJ, 902, 124

Carlsten S. G., Greene J. E., Peter A. H. G., Beaton R. L., Greco J. P., 2021, ApJ, 908, 109

Chabrier G., 2001, ApJ, 554, 1274

Chambers K. C. et al., 2016, preprint (arXiv:1612.05560)

Chau A., Mayer L., Governato F., 2017, ApJ, 845, 17

Chen Y., Girardi L., Bressan A., Marigo P., Barbieri M., Kong X., 2014, MNRAS, 444, 2525

Child H. L., Habib S., Heitmann K., Frontiere N., Finkel H., Pope A., Morozov V., 2018, ApJ, 859, 55

Crnojević D. et al., 2019, ApJ, 872, 80

Dalcanton J. J. et al., 2009, ApJS, 183, 67
Danieli S., van Dokkum P., Merritt A., Abraham R., Zhang J., Karachentsev
    I. D., Makarova L. N., 2017, ApJ, 837, 136
Davis A. B. et al., 2021, MNRAS, 500, 3854
Dejonghe H., 1987, MNRAS, 224, 13
Delfino F. M., Scoccola C. G., Cora S. A., Vega-Martinez C. A., Gargiulo I.
    D., 2021, preprint (arXiv:2102.01837)
Diemer B., 2021, ApJ, 909, 112
Dolphin A. E., 2002, MNRAS, 332, 91
Dooley G. A., Peter A. H. G., Yang T., Willman B., Griffen B. F., Frebel A.,
    2017a, MNRAS, 471, 4894
Dooley G. A., Peter A. H. G., Carlin J. L., Frebel A., Bechtol K., Willman
    B., 2017b, MNRAS, 472, 1060
Drakos N. E., Taylor J. E., Benson A. J., 2020, MNRAS, 494, 378
Drlica-Wagner A. et al., 2020, ApJ, 893, 47
Fillingham S. P., Cooper M. C., Pace A. B., Boylan-Kolchin M., Bullock J.
    S., Garrison-Kimmel S., Wheeler C., 2016, MNRAS, 463, 1916
Flewelling H. A. et al., 2020, ApJS, 251, 7
Gaia Collaboration, 2018, A&A, 616, A1
Gallart C., Aparicio A., Vilchez J. M., 1996, AJ, 112, 1928
Gao L., White S. D. M., Jenkins A., Stoehr F., Springel V., 2004, MNRAS,
    355, 819
Gao L., Navarro J. F., Frenk C. S., Jenkins A., Springel V., White S. D. M.,
    2012, MNRAS, 425, 2169
García-Benito R., Delgado R. M. G., Pérez E., Fernandes R. C., Sánchez S.
    F., de Amorim A. L., 2019, A&A, 621, A120
Garling C. T., Peter A. H. G., Kochanek C. S., Sand D. J., Crnojević D., 2020,
    MNRAS, 492, 1713
Garrison-Kimmel S., Bullock J. S., Boylan-Kolchin M., Bardwell E., 2017,
    MNRAS, 464, 3108
Geha M. et al., 2017, ApJ, 847, 4
Gerke J. R., Kochanek C. S., Stanek K. Z., 2015, MNRAS, 450, 3289
Gilman D., Birrer S., Nierenberg A., Treu T., Du X., Benson A., 2020,
    MNRAS, 491, 6077
Gruen D., Seitz S., Bernstein G. M., 2014, PASP, 126, 158
Gunn J. E., Gott III J. R., 1972, ApJ, 176, 1
Han J., Cole S., Frenk C. S., Jing Y., 2016, MNRAS, 457, 1208
Häußler B. et al., 2013, MNRAS, 430, 330
Hill J. M., Green R. F., Ashby D. S., Brynnel J. G., Cushing N. J., Little J.,
    Slagle J. H., Wagner R. M., 2010, in Proc. SPIE Conf. Ser. Vol. 7733,
    Ground-Based and Airborne Telescopes III. SPIE, Bellingham, p. 77330C
Jacobs B. A., Rizzi L., Tully R. B., Shaya E. J., Makarov D. I., Makarova L.,
    2009, AJ, 138, 332
Jethwa P., Erkal D., Belokurov V., 2018, MNRAS, 473, 2060
Jiang F., van den Bosch F. C., 2014, MNRAS, 440, 193
Jiang F., van den Bosch F. C., 2016, MNRAS, 458, 2848
Jiang F. et al., 2019, MNRAS, 488, 4801
Jiang F., Dekel A., Freundlich J., van den Bosch F. C., Green S. B., Hopkins
    P. F., Benson A., Du X., 2021, MNRAS, 502, 621
Jordi K., Grebel E. K., Ammon K., 2006, A&A, 460, 339
Karaali S., Bilir S., Tunçel S., 2005, Publ. Astron. Soc. Aust., 22, 24
Karachentsev I. D., Kaisin S. S., 2007, AJ, 133, 1883
Karachentsev I. D. et al., 2002, A&A, 383, 125
Karachentsev I. D., Makarov D. I., Kaisina E. I., 2013, AJ, 145, 101
Kennedy R., Frenk C., Cole S., Benson A., 2014, MNRAS, 442, 2487
Kereš D., Katz N., Fardal M., Davé R., Weinberg D. H., 2009, MNRAS, 395,
    160
Kim S. Y., Peter A. H. G., Hargis J. R., 2018, Phys. Rev. Lett., 121, 211302
Kochanek C. S., Beacom J. F., Kistler M. D., Prieto J. L., Stanek K. Z.,
    Thompson T. A., Yüksel H., 2008, ApJ, 684, 1336
Komatsu E. et al., 2011, ApJS, 192, 18
Lang D., Hogg D. W., Mierle K., Blanton M., Roweis S., 2010, AJ, 139, 1782
Leroy A. K. et al., 2019, ApJS, 244, 24
Lovell M. R., 2020, MNRAS, 493, L11
Lovell M. R. et al., 2017, MNRAS, 468, 4285
McQuinn K. B. W. et al., 2010, ApJ, 721, 297
Mao Y.-Y., Geha M., Wechsler R. H., Weiner B., Tollerud E. J., Nadler E. O.,
    Kallivayalil N., 2021, ApJ, 907, 85

Marigo P. et al., 2017, ApJ, 835, 77
Martin N. F., de Jong J. T. A., Rix H.-W., 2008, ApJ, 684, 1075
Martínez-Delgado D. et al., 2012, ApJ, 748, L24
Mayer L., Mastropietro C., Wadsley J., Stadel J., Moore B., 2006, MNRAS,
    369, 1021
More S., Diemer B., Kravtsov A. V., 2015, ApJ, 810, 36
Moster B. P., Naab T., White S. D. M., 2013, MNRAS, 428, 3121
Moster B. P., Naab T., Lindström M., O'Leary J. A., 2021, MNRAS, 507,
    2115
Müller O., Jerjen H., 2020, A&A, 644, A91
Müller O., Scalera R., Binggeli B., Jerjen H., 2017, A&A, 602, A119
Müller O., Jerjen H., Binggeli B., 2018, A&A, 615, A105
Müller O., Rejkuba M., Pawlowski M. S., Ibata R., Lelli F., Hilker M., Jerjen
    H., 2019, A&A, 629, A18
Muñoz R. R., Côté P., Santana F. A., Geha M., Simon J. D., Oyarzún G. A.,
    Stetson P. B., Djorgovski S. G., 2018, ApJ, 860, 66
Nadler E. O., Mao Y.-Y., Green G. M., Wechsler R. H., 2019, ApJ, 873, 34
Nadler E. O. et al., 2020, ApJ, 893, 48
Nadler E. O., Birrer S., Gilman D., Wechsler R. H., Du X., Benson A.,
    Nierenberg A. M., Treu T., 2021, ApJ, 917, 7
Navarro J. F., 2018, in McQuinn K., Stierwalt S., eds, Proc. IAU Symp. 344,
    Dwarf Galaxies: From the Deep Universe to the Present. Cambridge Univ.
    Press, Cambridge
Neustadt J. M. M., Kochanek C. S., Stanek K. Z., Basinger C. M.,
    Jayasinghe T., Garling C. T., Adams S. M., Gerke J., 2021, preprint
    (arXiv:2104.03318)
Newton O., Leo M., Cautun M., Jenkins A., Frenk C. S., Lovell M. R., Helly
    J. C., Benson A. J., 2021, JCAP, 2021, 062
Nierenberg A. M., Auger M. W., Treu T., Marshall P. J., Fassnacht C. D.,
    Busha M. T., 2012, ApJ, 752, 99
Nierenberg A. M., Treu T., Menci N., Lu Y., Torrey P., Vogelsberger M.,
    2016, MNRAS, 462, 4473
Olsen K. A. G., Blum R. D., Rigaut F., 2003, AJ, 126, 452
Peñarrubia J., Navarro J. F., McConnachie A. W., 2008, ApJ, 673, 226
Peñarrubia J., Benson A. J., Walker M. G., Gilmore G., McConnachie A. W.,
    Mayer L., 2010, MNRAS, 406, 1290
Peng C. Y., Ho L. C., Impey C. D., Rix H.-W., 2010, AJ, 139, 2097
Plummer H. C., 1911, MNRAS, 71, 460
Ragazzoni R. et al., 2006, in Proc. SPIE Conf. Ser. Vol. 6267. SPIE,
    Bellingham, p. 626710
Reddick R. M., Wechsler R. H., Tinker J. L., Behroozi P. S., 2013, ApJ, 771,
    30
Rich R. M., Collins M. L. M., Black C. M., Longstaff F. A., Koch A., Benson
    A., Reitzel D. B., 2012, Nature, 482, 192
Roberts D. M., Nierenberg A. M., Peter A. H. G., 2021, MNRAS, 502, 1205
Rodríguez-Puebla A., Primack J. R., Avila-Reese V., Faber S. M., 2017,
    MNRAS, 470, 651
Sabbi E. et al., 2018, ApJS, 235, 23
Safarzadeh M., Spergel D. N., 2020, ApJ, 893, 21
Sand D. J. et al., 2014, ApJ, 793, L7
Schlafly E. F., Finkbeiner D. P., 2011, ApJ, 737, 103
Schlegel D. J., Finkbeiner D. P., Davis M., 1998, ApJ, 500, 525
Simha V., Cole S., 2017, MNRAS, 472, 1392
Smercina A., Bell E. F., Price P. A., D'Souza R., Slater C. T., Bailin J.,
    Monachesi A., Nidever D., 2018, ApJ, 863, 152
Somerville R. S. et al., 2018, MNRAS, 473, 2714
Speziali R. et al., 2008, in McLean I. S., Casali M. M., eds, Proc. SPIE
    Conf. Ser. Vol. 7014, Ground-Based and Airborne Instrumentation for
    Astronomy II. SPIE, Marseille, p. 70144T
Stern J., Fielding D., Faucher-Giguère C.-A., Quataert E., 2020, MNRAS,
    492, 6042
Stetson P. B., 1987, PASP, 99, 191
Stetson P. B., 1992, in Worrall D. M., Biemesderfer C., Barnes J., eds, ASP
    Conf. Ser. Vol. 25, Astronomical Data Analysis Software and Systems I.
    Astron. Soc. Pac., San Francisco, p. 297
Stetson P. B., 1994, PASP, 106, 250
The DES Collaboration, 2015a, ApJ, 807, 50
The DES Collaboration, 2015b, ApJ, 813, 109

Toloba E., Guhathakurta P., Romanowsky A. J., Brodie J. P., Martínez-Delgado D., Arnold J. A., Ramachandran N., Theakanath K., 2016, ApJ, 824, 35

Tonnesen S., 2019, ApJ, 874, 161

Tonry J. L. et al., 2012, ApJ, 750, 99

van den Bosch F. C., Ogiya G., 2018, MNRAS, 475, 4066

van den Bosch F. C., Ogiya G., Hahn O., Burkert A., 2018, MNRAS, 474, 3043

Walsh S. M., Willman B., Jerjen H., 2009, AJ, 137, 450

Wang Y., Nadler E. O., Mao Y.-Y., Adhikari S., Wechsler R. H., Behroozi P., 2021, ApJ, 915, 116

Weisz D. R. et al., 2011, ApJ, 739, 5

Woo J., Courteau S., Dekel A., 2008, MNRAS, 390, 1453

Zheng Z., Weinberg D. H., 2007, ApJ, 659, 1

Zheng Z. et al., 2005, ApJ, 633, 791

This paper has been typeset from a TeX/LaTeX file prepared by the author.